



Repositorio Institucional de la Universidad Autónoma de Madrid

<https://repositorio.uam.es>

Esta es la **versión de autor** del artículo publicado en:

This is an **author produced version** of a paper published in:

Applied Physics Letters 12.16 (2018): 1611901

DOI: <http://doi.org/10.1063/1.5024683>

Copyright: © 2018 The Author (s)

El acceso a la versión del editor puede requerir la suscripción del recurso
Access to the published version may require subscription

Spectroscopic ellipsometry study of $\text{Cu}_2\text{ZnSnS}_4$ bulk poly-crystals

**S. Levchenko^{a*}, E. Hajdeu-Chicarosh^b, E. Garcia-Llamas^c, R. Caballero^c, R. Serna^d,
I. V. Bodnar^e, I. A. Victorov^e, M. Guc^b, J. M. Merino^c, A. Pérez-Rodríguez^{f,g},
E. Arushanov^b, and M. León^c**

^a*Helmholtz-Zentrum Berlin für Materialien und Energie, Berlin, Germany*

^b*Institute of Applied Physics, Chisinau, Moldova*

^c*Department of Applied Physics M12, Universidad Autónoma de Madrid, Madrid, Spain*

^d*Laser Processing Group, Instituto de Optica, IO, CSIC, Madrid, Spain*

^e*Belarusian State University of Informatics and Radioelectronics, Minsk, Belarus*

^f*IREC, Catalonia Institute for Energy Research, Sant Adrià del Besòs (Barcelona), Spain*

^g*IN²UB, Departament d'Enginyeria Electrònica i Biomèdica, Universitat de Barcelona, Barcelona, Spain*

*Corresponding author: S. Levchenko; email sergiu.levcenco@helmholtz-berlin.de

The linear optical properties of $\text{Cu}_2\text{ZnSnS}_4$ bulk poly-crystals have been investigated using spectroscopic ellipsometry in the range 1.2 – 4.6 eV at room temperature. The characteristic features identified in the optical spectra are explained by using the Adachi analytical model for the interband transitions at the corresponding critical points in the Brillouin zone (BZ). The experimental data have been modeled over the entire spectral range taking into account the lowest E_0 transition near the fundamental absorption edge, and E_{1A} and E_{1B} higher energy interband transitions. In addition, the spectral dependences of the refractive index, extinction coefficient, absorption coefficient, and normal-incidence reflectivity values have been determined and are provided since they are essential data for the design of $\text{Cu}_2\text{ZnSnS}_4$ based optoelectronic devices.

In the span of the last decade, much progress has been made in the kesterite based $\text{Cu}_2\text{ZnSnS}_4$ (CZTS) thin film solar cells. This is because kesterites show excellent properties as absorber materials such as an optimal band gap of ~ 1.5 eV¹⁻³ which can be tuned by adjusting anion and cation compositions^{4,5} and a high optical absorption coefficient^{6,7} over $\sim 10^4$ cm⁻¹. Moreover, the kesterites are constituted by low-cost elements with low toxicity and abundant in the Earth's crust, which allows avoiding the use of critical raw materials.

The best solar cell efficiency has been reached values of 9 % for CZTS based solar cells⁸ and 12.6 % for the alloyed kesterite photovoltaic devices.⁵ Other possible applications of CZTS range from utilization as a wide-gap p-type thermoelectric material⁹ to a photoelectrode layer in the water splitting devices.¹⁰

Despite of the considerable efforts aimed at the development of kesterite thin film technology and the photovoltaic conversion improvements, there is still a limited number of works centered on their fundamental material properties. Most reports deal with the structural investigation,^{11,12} the theoretical calculation of electronic band structure and point defects,^{7,13-15} as well as the analysis of electrical transport,^{16,17} vibrational^{18,19} and optical properties.^{1-3,7,13} However, for the optoelectronic applications it is mandatory to have a deeper and more accurate knowledge on the optical properties in a wide photon energy range. An examination of the spectroscopic ellipsometry (SE) literature shows that the dielectric function data, ϵ , have been reported for CZTS thin films.^{7,20,21} However the optical response of the thin film has been often treated with the multi-layer stack model composed from three to six sub layers,^{7,21} which has a limited accuracy. In this context the data obtained from the bulk poly-crystals in principle should be more reliable and have a greater value for the actual polycrystalline devices design over the measurements on single-crystalline material that show strong polarization dependence of the dielectric function. In this letter, from the SE measurements over the range from 1.2 to 4.6 eV we determine the intrinsic dielectric function of CZTS bulk poly-crystals by taking into account the presence of a roughness layer on the surface of the specimens induced by chemical and mechanical sample preparation procedures. The dispersion of the dielectric function has been parameterized based on the Adachi model for the interband transitions, which in turn enables to calculate the CZTS optical constants over the wide spectral range relevant for device applications.

$\text{Cu}_2\text{ZnSnS}_4$ crystals were grown by the modified Bridgman method.³ The chemical composition was investigated by Energy Dispersive X-ray microanalysis (EDX) measurements (Oxford instruments, model INCA Xsight) inside a Hitachi S-3000N scanning electron microscope. The Cu/(Zn+Sn) ratio varies from 0.8 to 1.1 and the Zn/Sn ratio lies in the range of 0.9 – 1.3 in the selected samples (Table I).

To determine the possible presence of secondary phases in CZTS poly-crystals we carried out Raman measurements by using a LabRam HR800-UV Horiba Jobin Yvon spectrometer coupled with a CCD detector. Under 532 nm excitation (Fig. 1 (a)) all the detected peaks, including the most intense peaks at 339 and 289 cm^{-1} , correspond to

vibrational modes of CZTS.^{18,19} The relatively low value of full width at half maximum of the most intense peaks ($\sim 9 \text{ cm}^{-1}$ in S1, $\sim 6 \text{ cm}^{-1}$ in S2 and $\sim 7 \text{ cm}^{-1}$ in S3), as well as the detection of the low intensity CZTS peaks denotes a good sample crystallinity. The spectra excited with He-Cd laser (line 325 nm) were used to exclude the possible presence of ZnS phase.²² Fig. 1 (b) shows that under the UV excitation an enhancement of the peak at 320 cm^{-1} and appearance of a small additional peak at 677 cm^{-1} occurred. The first of them is identified with a CZTS characteristic mode,¹⁸ while the second is attributed to the second order of the main CZTS peak.¹⁹ Experimentally, we have observed that excitation of the Raman spectra with NIR laser (line 785 nm) improves the detection of SnS and Cu_2SnS_3 phases, as this laser line is closer to the resonant conditions for these compounds. Fig. 1 (c) shows a typical spectrum obtained under NIR excitation, but none of the peaks could be attributed to the SnS or Cu_2SnS_3 phases.^{23,24} Finally, for any of the used excitation conditions it has not been possible to observe the presence of Cu_{2-x}S phase, which has a dominant peak at 475 cm^{-1} .²⁵ According to the Raman data, no evidence has been obtained on the presence of any secondary phase in the investigated samples.

The optical response of CZTS poly-crystals is analyzed by considering a three-phase model²⁶ composed of air, rough surface layer and bulk material. We have modeled the thin roughness layer as a mixture of air voids and bulk CZTS with the fixed 50 % ratio of each component. The Bruggeman effective medium approximation (EMA) was applied to describe dielectric function of this effective medium.²⁷ Thus, our model includes thickness of the roughness surface layer as an additional parameter in comparison to the ideal two-phase model.²⁸

Following Adachi,^{29,30} we adopted the model for the dielectric function (MDF) to describe the complex dielectric function, $\varepsilon(E) = \varepsilon_1(E) + i\varepsilon_2(E)$, as a function of the photon energy, E , over the spectral range from the absorption edge up to 4.6 eV in CZTS. This is similar to the previous SE studies on $\text{Cu}_2\text{Zn}(\text{Sn,Ge})\text{Se}_4$ quaternaries with tetragonal type structure.^{31,32} The general expression for the $\varepsilon(E)$ includes three terms:

$$\varepsilon(E) = \varepsilon^{(0)}(E) + \varepsilon^{(1)}(E) + \varepsilon_{1\infty}, \quad (1)$$

where $\varepsilon^{(0)}(E)$ is the contribution from the electronic transitions near the band gap region, $\varepsilon^{(1)}(E)$ is the combined contribution from the interband transitions near the 2D- M_1 and the 2D- M_0 critical points (CP's), and $\varepsilon_{1\infty}$ accounts for the higher energy CP's outside the experimental range.²⁹

The assumptions on the parabolic nature for the valence and conduction bands for the

lowest energy transitions and the 3D M_0 type character of the CP result in $\varepsilon^{(0)}(E)$ of the form:

$$\varepsilon^{(0)}(E) = AE_0^{-3/2} \chi_0^{-2} (2 - (1 + \chi_0)^{1/2} - (1 - \chi_0)^{1/2}) \quad (2)$$

with $\chi_0 = (E + i\Gamma_0)/E_0$, where A and Γ_0 are the strength and the broadening energy of the E_0 transition, respectively.

The $\varepsilon^{(1)}(E)$ component is given by:

$$\varepsilon^{(1)}(E) = B_{1A} \left[1 - (E/E_{1A})^2 - i(E/E_{1A})\Gamma_{1A} \right]^{-1} - B_{1B} \chi_{1B}^{-2} \ln(1 - \chi_{1B}^2) \quad (3)$$

where B_{1A} and Γ_{1A} are the strength and broadening parameters of the E_{1A} transition at the 2D- M_1 CP and $\chi_{1B} = (E + i\Gamma_{1B})/E_{1B}$, with B_{1B} and Γ_{1B} the strength and broadening energy of the E_{1B} transition near 2D- M_0 CP.

To have a more accurate description of $\varepsilon(E)$ in Eq. (1), a Gaussian type broadening mechanism has been assumed for the interband transitions, after Kim,³³

$$\Gamma_i'(E) = \Gamma_i \exp\left(-s_i \left(\frac{E - E_i}{\Gamma_i}\right)^2\right) \quad (4)$$

where s_i is the non-dimensional parameter, Γ_i is the broadening parameter, E_i is the transition energy, and i is 0, 1A or 1B.

The use of the simulated annealing (SA) algorithm³⁴ has enabled us to perform a global minimization procedure and to calculate the MDF parameters. The following objective function³⁵ was selected in the minimized routine:

$$F = \sum_{i=1}^N \left(\left| \frac{\Delta(E_i)}{\Delta_{exp}(E_i)} - 1 \right| + \left| \frac{\Psi(E_i)}{\Psi_{exp}(E_i)} - 1 \right| \right)^2 \quad (5)$$

where $\Delta_{exp}(E_i)$, $\Psi_{exp}(E_i)$, and $\Delta(E_i)$, $\Psi(E_i)$ are the experimental and calculated values of the ellipsometry parameters at the E_i point, respectively, and N is the number of the experimental points.

The optical measurements were performed with a variable-angle spectroscopic ellipsometer (J. A. Woollam VASE) at 300 K and at two incidence angles Φ , 60° and 70° in the photon energy range 1.2 – 4.6 eV. The information on the preparation of good quality “pure” sample surface can be found in Ref. 36. Fig. 2 shows the plot of typical experimental (Δ_{exp} , Ψ_{exp}) curves as a function of E for samples S1 and S3. Over the measured spectral range the experimental results agree well with the theoretical predictions for the interband transitions (Eqs. (1) – (4)), which are also plotted in Fig. 2 as solid lines. The relative errors

for the obtained (Δ , Ψ)-ellipsometry parameters ranges between 2 % and 4 %. Table II lists the MDF parameters for the different samples. The calculated values of the surface layer thickness are in the range 6 – 8 nm, which are acceptable values taking into account the specific surface preparation for the SE measurements.³⁷ From the global fitting procedure the value of the $\varepsilon_{1\infty}$ parameter was found negligibly small and was omitted in Table I. We found that introducing the Gaussian broadening mechanism (Eq. (4)) for the E_0 transition does not have any influence on the value of F (Eq. (5)) in contrast to E_{1A} and E_{1B} CP's.

Fig. 3 (a) shows the calculated real and imaginary parts of the ε -function for the three samples. The line shape of the $\varepsilon(E)$ -curves for S1 and S3 samples are quite similar but shifted by about 0.1 eV in energy. This is not an unexpected result as a spectral similarity can already be noticed in the raw (Δ , Ψ) data (Fig. 2). The $\varepsilon_2(E)$ from the S2 sample resembles the $\varepsilon_2(E)$ shapes of S1 and S3 samples, too, but composed of broadened features. Quantitatively, the similarity between the CZTS samples can be concluded from the calculated MDF parameters (Table II). We can also define analytically the high frequency dielectric constant, ε_∞ , for CZTS. Developing Eq. (1) for $E \approx 0$ and assuming $\varepsilon_{1\infty} \approx 0$ we get $\varepsilon_\infty \approx A / (4 \times E_0^{1.5}) + B_{1A} + B_{1B}$. The obtained values of ε_∞ are in the range 7.0 – 7.2 for the studied samples, while the recent *ab-initio* calculations give close but lower values of 6.5 – 6.8 depending on the employed functional.⁷

Let us now consider the obtained energies of the interband transitions. For the E_0 transition we get a value from 1.53 to 1.67 eV, which can be assigned to the transition between the valence band maximum (VBM) to the conduction band minimum (CBM) at the $\Gamma(0,0,0)$ point in the BZ.^{7,13} These values reasonably agree with the band gap values of 1.51 – 1.59 eV on thin films derived from the SE,^{7,21} but larger than the earlier reported 1.30 eV.²⁰ Notably, the decrease in E_0 correlates with the reduction in the Cu/(Zn+Sn) ratio (Table 1). However, this tendency is opposite to those found in $\text{Cu}_2\text{ZnSnSe}_4$, where the band gap increases with copper deficiency.³⁸ On the other hand, the Cu-Zn lattice disorder in CZTS can induce a change in the band gap of about 0.2 eV.³⁹ According to this concept, an increase of the band gap is related to an increase of degree of ordering in the samples. Unfortunately, the amount of the Cu-Zn lattice disorder is not known in the studied polycrystals and the actual mechanism responsible for the E_0 variation cannot be determined at this stage.

The E_{1A} CP energies are obtained in the range 2.86 – 2.97 eV which can be attributed to the transition from VBM to the second conduction band at $\Gamma(0,0,0)$ point¹³ or to

transitions at P(1/2,1/2,1/2) point in the BZ.⁷ In the room temperature SE study on thin films,⁷ a value of 3.09 eV is derived from $d^2\varepsilon(E)/dE^2$ spectra, while the thermorefectance on crystals¹³ at 25 K resulted in a dominant transition with 3.3 eV. Interestingly, the transition of the E_{1A} CP is about 1.3 eV higher in energy than the E_0 CP for all the investigated samples. A slightly larger difference (1.4 eV) has been also found in the SE study from sulfoselenide thin films.⁷

The high-energy transition of the E_{1B} CP is found to be 4.8 – 5.0 eV and contains numerous contributions with different types of transitions occurring over a wide region of BZ, so the amplitudes of these CP structures become relatively large due to the close locations of multiple transitions. Tentatively E_{1B} CP can be associated with the transition at T(0,0,1) point in the BZ.¹³ According to the thermorefectance at 25 K the energy of this transition is 4.8 eV.¹³ However, it should be noted that our experimental spectral range limits the accurate determination of the E_{1B} transition parameters and higher energy data points are necessary to better analyze its characteristics.

In view of the application, design and optimization of the CZTS solar cells as a multilayer thin film system we present the dielectric function related optical constants such as the refractive index and extinction coefficient (Fig. 3 (b)), as well as the normal incidence reflectivity and absorption coefficient (Figs. 3 (c) and 3 (d)). Similar to the $\varepsilon(E)$ spectra the optical constants reveal distinct structures near the analyzed E_0 , E_{1A} and E_{1B} CP's.

In conclusion, the intrinsic optical constants for $\text{Cu}_2\text{ZnSnS}_4$ polycrystalline samples, grown by the modified Bridgman method, have been determined by using three-phase model from the SE measurements in the 1.2 – 4.6 eV photon energy range. Multi-excitation wavelength Raman scattering measurements support the high crystalline quality of the bulk samples and show no evidence of the presence of secondary phases. To describe the optical spectra we propose an application of the Adachi's model, which includes the E_0 , E_{1A} and E_{1B} interband transition contributions to the dielectric function. The obtained analytical description of the dielectric function will be useful for the design of optoelectronic devices and for the analysis of optical measurements of multilayer structures based on the $\text{Cu}_2\text{ZnSnS}_4$ material.

The research leading to the presented results has been partially supported by the European project INFINITE-CELL (ref. H2020-MSCA-RISE-2017-777968, 2017-2021, www.infinite-cell.eu) and the Spanish MINECO projects "WINCOST" (ENE2016-80788-

C5-2-R) and PHOTOMANA (TEC2015-69916-C2-1-R). Authors from the Institute of Applied Physics appreciate the financial supports from STCU 6224 and from the Institutional Project CSSDT 15.817.02.04A.

- ¹ P. K. Sarswat and M. L. Free, *Physica B* **407**, 108 (2012).
- ² S. Levchenko, D. Dumcenco, Y. P. Wang, Y. S. Huang, C. H. Ho, E. Arushanov, V. Tezlevan, and K. K. Tiong, *Opt. Mater.* **34**, 1362 (2012).
- ³ I. V. Bodnar, *Semiconductors* **49**, 582 (2015).
- ⁴ C. J. Hages, S. Levchenko, C. K. Miskin, J. H. Alsmeier, D. Abou-Ras, R. G. Wilks, M. Bär, T. Unold, and R. Agrawal, *Prog. Photovolt: Res. Appl.* **23**, 376 (2015).
- ⁵ W. Wang, M. T. Winkler, O. Gunawan, T. Gokmen, T. K. Todorov, Y. Zhu, and D. B. Mitzi, *Adv. Energy Mater.* **4**, 1301465 (2013).
- ⁶ E. Garcia-Llamas, J. M. Merino, R. Serna, X. Fontané, I. A. Victorov, A. Pérez-Rodríguez, M. León, I. V. Bodnar, V. Izquierdo-Roca, and R. Caballero, *Sol. Energy Mater. Sol. Cells* **158**, 147 (2016).
- ⁷ S. Y. Li, S. Zamulko, C. Persson, N. Ross, J. K. Larsen, and C. Platzer-Björkmann, *Appl. Phys. Lett.* **110**, 021905 (2017).
- ⁸ K. Sun, C. Yan, F. Liu, J. Huang, F. Zhou, J. A. Stride, M. Green, and X. Hao, *Adv. Energy Mater.* **6**, 1600046 (2016).
- ⁹ M. L. Liu, F. Q. Huang, L. D. Chen, and I. W. Chen, *Appl. Phys. Lett.* **94**, 202103 (2009).
- ¹⁰ D. Yokoyama, T. Minegishi, K. Jimbo, T. Hisatomi, G. Ma, M. Katayama, J. Kubota, H. Katagiri, and K. Domen, *Appl. Phys. Express.* **3**, 101202 (2010).
- ¹¹ S. Schorr, *Thin Solid Films* **515**, 5985 (2007).
- ¹² A. Lafond, L. Choubrac, C. Guillot-Deudon, P. Fertey, M. Evaina, and S. Jobic, *Acta Cryst. B* **70**, 390 (2014).
- ¹³ S. Ozaki, K. Hoshina, and Y. Usami, *Phys. Status Solidi C* **12**, 717 (2015).
- ¹⁴ A. Walsh, S. Chen, S. H. Wei, and X. G. Gong, *Adv. Energy Mater.* **2**, 400 (2012).
- ¹⁵ S. Chen, A. Walsh, X. G. Gong, and S. H. Wei, *Adv. Mater.* **25**, 1522 (2013).
- ¹⁶ A. Nagaoka, H. Miyake, T. Taniyama, K. Kakimoto, and K. Yoshino, *Appl. Phys. Lett.* **103**, 112107 (2013).
- ¹⁷ E. Lahderanta, M. Guc, M. A. Shakhov, E. Arushanov, and K. G. Lisunov, *J. Appl. Phys.* **120**, 035704 (2016).
- ¹⁸ M. Guc, S. Levchenko, I. V. Bodnar, V. Izquierdo-Roca, X. Fontane, L. V. Volkova, E. Arushanov, and A. Pérez-Rodríguez, *Sci. Rep.* **6**, 19414 (2016).

- ¹⁹ M. Dimitrievska, A. Fairbrother, X. Fontane, T. Jawhari, V. Izquierdo-Roca, E. Saucedo, and A. Perez-Rodriguez, *Appl. Phys. Lett.* **104**, 021901 (2014).
- ²⁰ J. Li, H. Du, J. Yarbrough, A. Norman, K. Jones, G. Teeter, F. Lewis Terry, and D. Levi, *Opt. Express* **20**, A327 (2012).
- ²¹ S. Y. Li, C. Hägglund, Y. Ren, J. J. Scragg, J. K. Larsen, C. Frisk, K. Rudisch, S. Englund, and C. Platzer-Björkmann, *Sol. Energy Mater. Sol. Cells* **149**, 170 (2016).
- ²² A. Fairbrother, V. Izquierdo-Roca, X. Fontané, M. Ibáñez, A. Cabot, E. Saucedo, and A. Pérez-Rodríguez, *CrystEngComm* **16**, 4120 (2014).
- ²³ H. R. Chandrasekhar, R. G. Humphreys, U. Zwick, and M. Cardona, *Phys. Rev. B* **15** 2177 (1977).
- ²⁴ F. Oliva, L. Arques, L. Acebo, M. Guc, Y. Sanchez, X. Alcobe, A. Pérez-Rodriguez, E. Saucedo, and V. Izquierdo-Roca, *J. Mater. Chem. A* **5**, 23863 (2017).
- ²⁵ M. Ishii, K. Shibata, and H. Nozaki, *J. Solid State Chem.* **105**, 504 (1993).
- ²⁶ S. H. Han, C. Persson, F. S. Hasoon, H. A. Al-Thani, A. M. Hermann, and D. H. Levi, *Phys. Rev. B* **74**, 085212 (2006).
- ²⁷ M. Erman, J. B. Theeten, P. Chambon, S. M. Kelso, and D. E. Aspnes, *J. Appl. Phys.* **56**, 2664 (1984).
- ²⁸ D. E. Aspnes and A. A. Studna, *Appl. Opt.* **14**, 1131 (1975).
- ²⁹ T. Kawashima, S. Adachi, H. Miyake, and K. Sugiyama, *J. Appl. Phys.* **84**, 5202 (1998).
- ³⁰ S. Adachi, T. Kimura, and N. Suzuki, *J. Appl. Phys.* **74**, 3435 (1993).
- ³¹ M. León, S. Levchenko, R. Serna, A. Nateprov, G. Gurieva, J. M. Merino, S. Schorr, and E. Arushanov, *Mater. Chem. Phys.* **141**, 58 (2013).
- ³² M. León, S. Levchenko, R. Serna, I. V. Bodnar, A. Nateprov, M. Guc, G. Gurieva, N. Lopez, J. M. Merino, R. Caballero, S. Schorr, A. Perez-Rodriguez, and E. Arushanov, *Appl. Phys. Lett.* **105**, 061909 (2014).
- ³³ C. C. Kim, J. W. Garland, H. Abad, and P. M. Racciah, *Phys. Rev. B* **45**, 11749 (1992).
- ³⁴ A. Corana, M. Marchesi, C. Martini, and S. Ridella, *ACM Trans. Math. Software* **13**, 262 (1987).
- ³⁵ A. B. Djurišić and E. H. Li, *J. Appl. Phys.* **85**, 2848 (1999).
- ³⁶ J. G. Albornoz, R. Serna, and M. León, *J. Appl. Phys.* **97**, 103515 (2006).
- ³⁷ R. Caballero, I. Victorov, R. Serna, J. M. Cano-Torres, C. Maffiotte, E. Garcia-Llamas, J. M. Merino, M. Valakh, I. Bodnar, and M. León, *Acta Mater.* **79**, 181 (2014).
- ³⁸ M. V. Yakushev, M. A. Sulimov, J. Márquez-Prieto, I. Forbes, J. Krustok, P. R. Edwards, V. D. Zhivulko, O. M. Borodavchenko, A. V. Mudryi, and R. W. Martin, *Sol. Energy Mater.*

Sol. Cells **168**, 69 (2017).

³⁹ J. J. Scragg, J. K. Larsen, M. Kumar, C. Persson, J. Sandler, S. Siebentritt, and C. Platzer-Björkmann, Phys. Status Solidi B **253**, 247 (2016).

Table I. Chemical composition of the CZTS samples used for the analysis.

Sample	Cu (at.%)	Zn (at.%)	Sn (at.%)	S (at.%)	Cu/(Zn+Sn)	Zn/Sn
S1	25.7	11.2	12.6	50.5	1.08	0.89
S2	23.6	12.4	12.5	51.5	0.95	1.01
S3	21.4	14.9	11.7	52.0	0.81	1.27

Table II. Model parameter values.

Parameters	A	E ₀	Γ ₀	B _{1A}	E _{1A}	Γ _{1A}	s _{1A}	B _{1B}	E _{1B}	Γ _{1B}	s _{1B}	Error	
Samples	(eV ^{1.5})	(eV)	(eV)		(eV)	(eV)			(eV)	(eV)		Ψ (%)	Δ (%)
S1	4.9	1.67	0.02	0.4	2.97	0.29	0.07	6.2	4.93	0.55	0.17	2.2	2.0
S2	5.8	1.62	0.03	0.5	2.92	0.34	0.10	5.9	4.80	0.62	0.15	3.3	3.8
S3	4.9	1.53	0.02	0.3	2.86	0.26	0.05	6.1	5.02	0.55	0.11	2.0	2.4

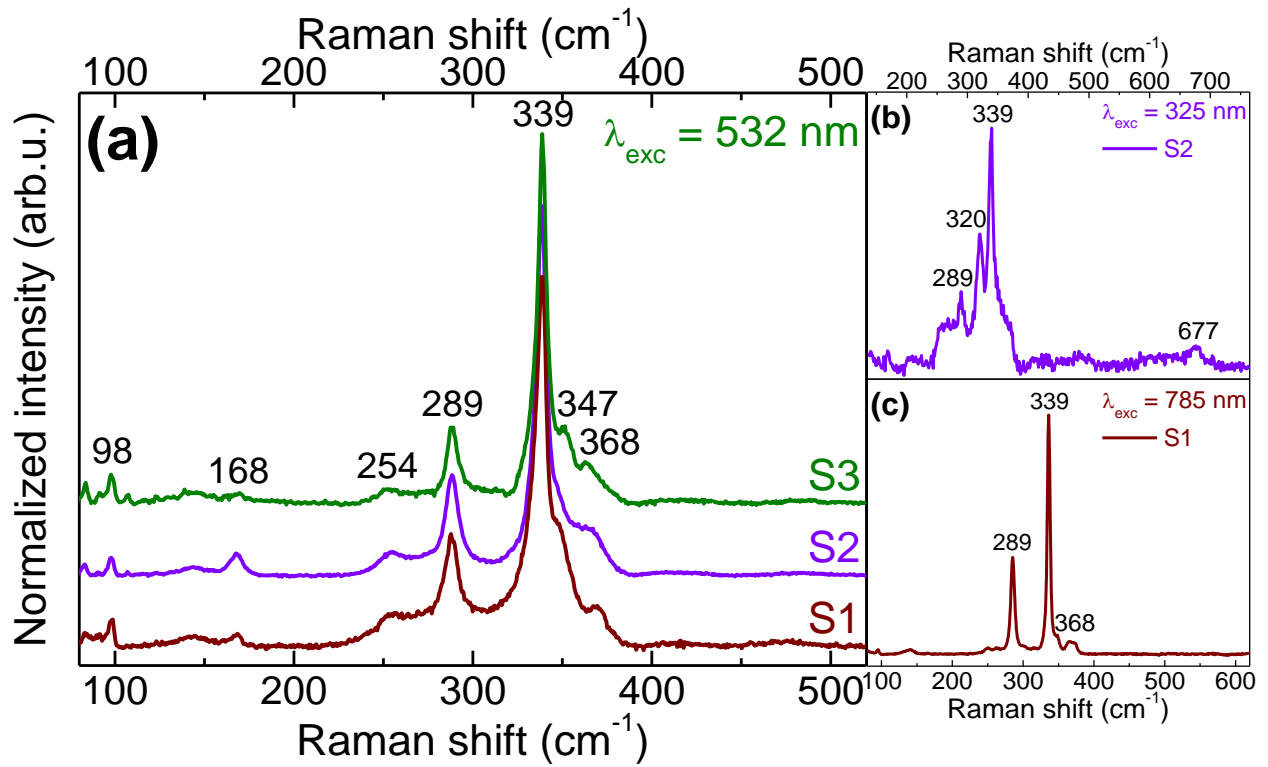


FIG. 1. Normalized Raman scattering spectra of investigated CZTS samples excited with 532 nm (a), 325 nm (b) and 785 nm (c) laser lines.

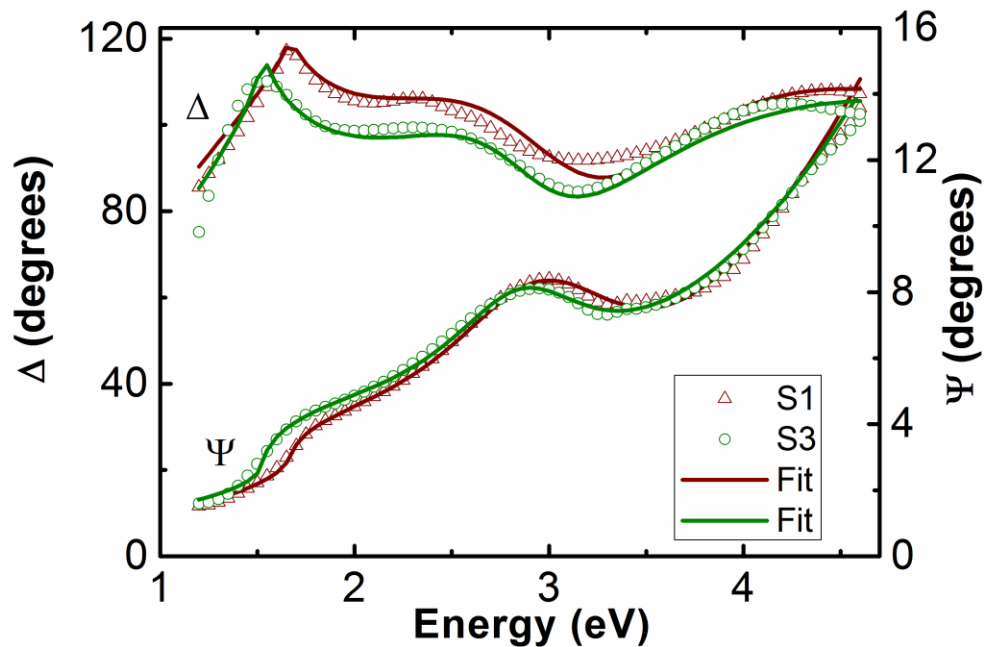


FIG. 2. Experimental Ψ and Δ spectra (points) and numerically calculated ones (solid lines), using three phase model (air, surface and bulk layers) for S1 and S3 samples of the CZTS poly-crystals.

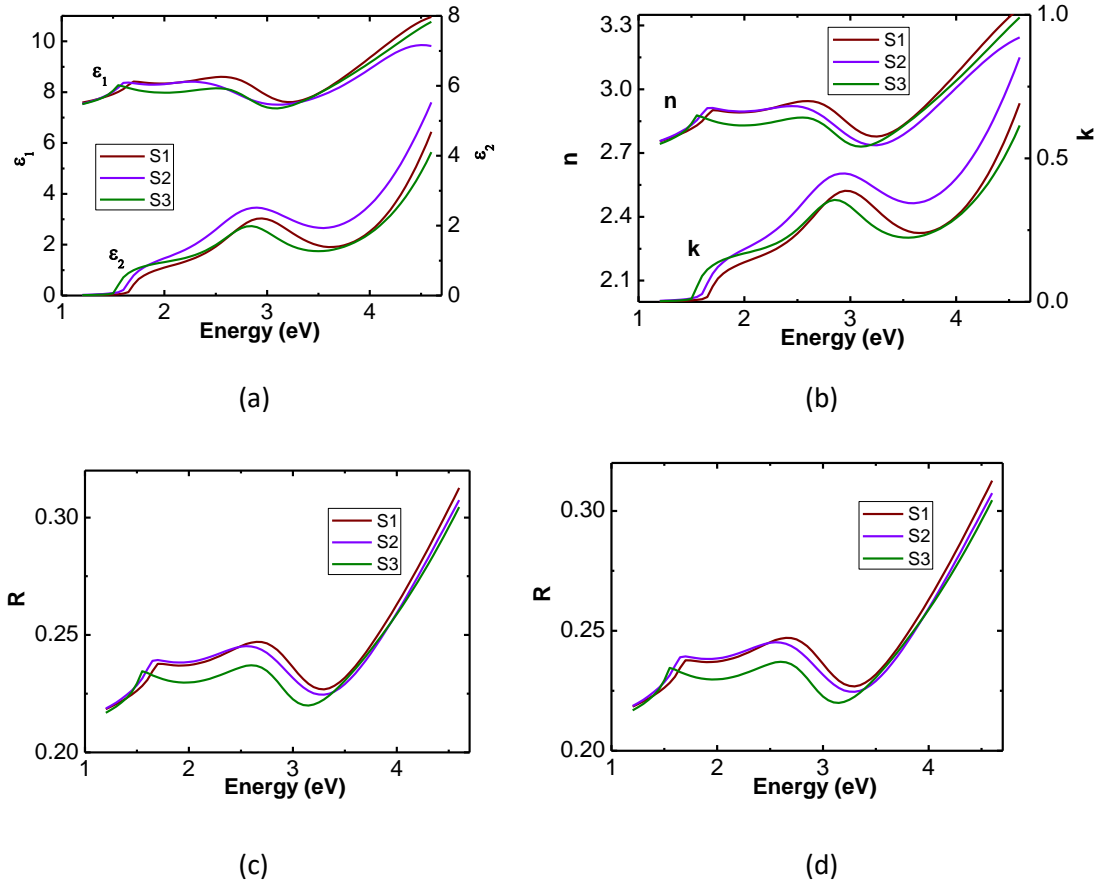


FIG. 3. Numerically calculated (a) dielectric function $\epsilon(E) = \epsilon_1(E) + i\epsilon_2(E)$, (b) extinction coefficient, k , and refractive index, n , (c) normal-incidence reflectivity, R , and (d) absorption coefficient, α , by using the MDF model and the SA algorithm for S1 – S3 samples of the CZTS poly-crystals.